

A NOVEL APPROACH TO CONSTRAIN THE MASS RATIO OF MINOR MERGERS IN ELLIPTICAL GALAXIES: APPLICATION TO NGC 4889, THE BRIGHTEST CLUSTER GALAXY IN COMA¹

MENG GU (顾梦)^{2,3}, LUIS C. HO³, CHIEN Y. PENG⁴ AND SONG HUANG (黄崧)^{2,3,5}
submitted to The Astrophysical Journal.

ABSTRACT

Minor mergers are thought to be important for the build-up and structural evolution of massive elliptical galaxies. In this work, we report the discovery of a system of four shell features in NGC 4889, one of the brightest members of the Coma cluster, using optical images taken with the *Hubble Space Telescope* and the Sloan Digital Sky Survey. The shells are well aligned with the major axis of the host and are likely to have been formed by the accretion of a small satellite galaxy. We have performed a detailed two-dimensional photometric decomposition of NGC 4889 and of the many overlapping nearby galaxies in its vicinity. This comprehensive model allows us not only to firmly detect the low-surface brightness shells, but, crucially, also to accurately measure their luminosities and colors. The shells are bluer than the underlying stars at the same radius in the main galaxy. We make use of the colors of the shells and the color-magnitude relation of the Coma cluster to infer the luminosity (or mass) of the progenitor galaxy. The shells in NGC 4889 appear to have been produced by the minor merger of a moderate-luminosity ($M_I \approx -18.7$ mag) disk (S0 or spiral) galaxy with a luminosity (mass) ratio of $\sim 90:1$ with respect to the primary galaxy. The novel methodology presented in this work can be exploited to decode the fossil record imprinted in the photometric substructure of other nearby early-type galaxies.

Subject headings: galaxies: elliptical and lenticular, cD — galaxies: evolution — galaxies: individual (NGC 4889) — galaxies: interactions — galaxies: photometry — galaxies: structure

1. INTRODUCTION

The evolution of massive early-type galaxies has always been a major concern in galaxy formation theory. This topic is becoming increasingly interesting due to the recent discovery of quiescent, compact early-type galaxies at high redshifts (Cimatti et al. 2004; Daddi et al. 2005; Trujillo et al. 2006). The population of “red nuggets,” which represent a unique phase of massive galaxy evolution (van Dokkum et al. 2010), is characterized by much smaller effective radius (Trujillo et al. 2006, 2007; Damjanov et al. 2011), higher central density (Szomoru et al. 2012), and possibly higher stellar velocity dispersion (Cappellari et al. 2009; Onodera et al. 2012) compared with nearby early-type galaxies at similar stellar mass. A significant fraction of these objects have disk-like morphologies (van der Wel et al. 2008).

Judging from their number density and stellar mass, red nuggets are considered probable progenitors of local massive early-type galaxies. To accomplish this transformation, the high- z compact objects on average need to double in stellar mass while increasing their effective radius by a factor of 3–5 since $z \approx 2.0$ (van Dokkum et al. 2010). To match the radial profiles of local massive elliptical galaxies, an extended stellar envelope needs to be gradually accumulated around the compact cores (Bezanson et al. 2009; Szomoru et al. 2012), whose high density implies a rapid phase of early, dissipative collapse. Moreover, most of the late-time growth needs to be accomplished without much significant gas dissipation to satisfy the observational constraint that early-type galaxies at $z \lesssim 2$ experience little observable star formation or black hole accretion (Bezanson et al. 2009; van Dokkum et al. 2010).

This two-phase evolutionary picture strongly challenges conventional models for the formation of elliptical galaxies, both monolithic collapse (Larson 1975) and binary merger (Toomre & Toomre 1972) scenarios. Instead, dissipationless processes such as “dry” mergers play a more central role. Considering the rarity of major (i.e. nearly equal-mass) dry mergers, late-time accretion of smaller stellar systems without significant cold gas content—minor dry mergers—appears to be the most promising pathway for achieving the inferred structural evolution (Naab et al. 2009). A series of simulations (Oser et al. 2010, 2012; Lackner et al. 2012) describes the two-phase formation scenario for massive early-type galaxies. According to this scenario, massive galaxies experience strong dissipational processes such as cold accretion (Dekel et al. 2009) and gas-rich (“wet”) mergers at high redshifts, resulting in early, rapid, concentrated mass growth. At lower redshifts, accretion of small systems dominates the evolution by building up the outer low-density envelopes around the initially compact cores (Naab et al. 2006, 2009; Oser et al. 2010). This picture has gained support from a variety of observations of nearby massive ellipticals (Coccato et al. 2010; Greene et al. 2012; Huang et al. 2013).

Located at the extreme high-mass end of the stellar mass function and the densest environments in the Universe, brightest cluster galaxies (BCGs) have been considered a special class of early-type galaxies that can be traced and compared across different redshifts (Sandage 1976; Postman & Lauer 1995). Motivated by the unique properties of BCGs, early ideas for their formation explored the role of X-ray-driven cooling flows (Silk 1976; Fabian 1994) and cannibalism (Ostriker & Tremaine 1975). The cooling flow picture emphasizes the im-

¹ Based on observations made with the NASA/ESA *Hubble Space Telescope*, obtained from the Data Archive at the Space Telescope Science Institute, which is operated by the Association of Universities for Research in Astronomy (AURA), Inc., under NASA contract NAS5-26555.

² School of Astronomy and Space Science, Nanjing University, Nanjing 210093, China

³ The Observatories of the Carnegie Institution for Science, 813 Santa Barbara Street, Pasadena, CA 91101, USA

⁴ Giant Magellan Telescope Organization, 251 South Lake Avenue, Suite 300, Pasadena, CA 91101, USA

⁵ Key Laboratory of Modern Astronomy and Astrophysics, Nanjing University, Nanjing 210093, China

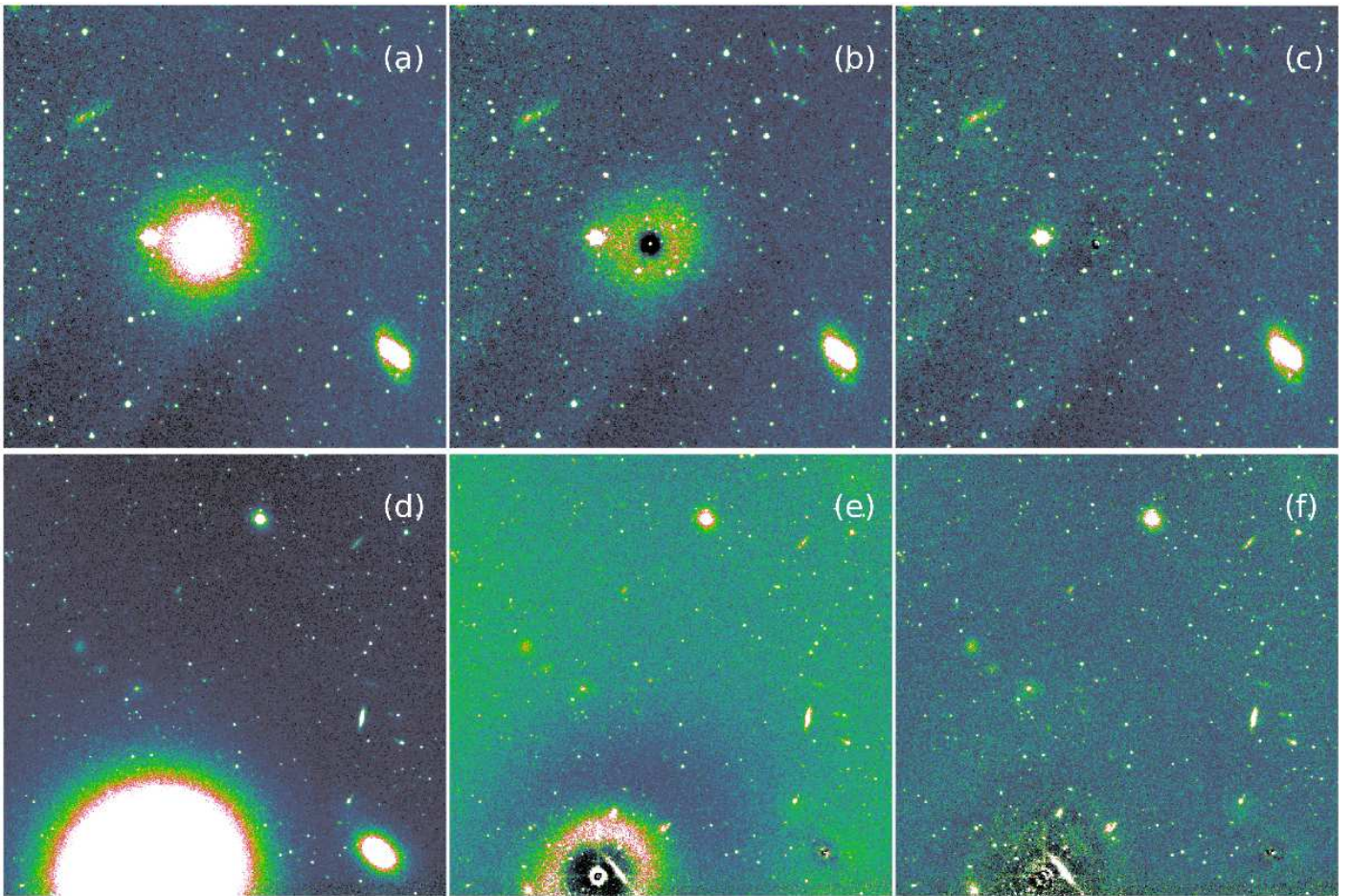


FIG. 1.— Examples of multiple-component fitting applied to sections of the *HST*/ACS F814W image that contain galaxies near NGC 4889. The top row shows a relatively simple galaxy (a), a single-component model (b), and a double-component model that finally does an adequate job in fitting the galaxy (c). The bottom row shows two more complicated cases (d), which are poorly fit even with two components (e), in the end requiring a model with six components for the larger galaxy and three components for the smaller system (f).

portant role of infalling gas in massive halos at high redshift: gas accretes directly onto the central galaxy located at the high-density, cooling center of X-ray-emitting halo, where stars can form rapidly. For the cannibalism scenario, the BCG mainly grows by swallowing its surrounding companions as they gradually fall into the central system under the influence of dynamical friction (White 1976; Ostriker & Hausman 1977). Modern scenarios for the formation of BCGs place greater emphasis on the role of galaxy mergers (e.g., Dubinski 1998) at different times (e.g., Khochfar & Silk 2006).

Numerical simulations and semi-analytic models suggest that the majority of the stars in nearby BCGs were formed in small systems very early ($z \approx 2-5$), later assembling into a larger entity via a series of mostly dry mergers (Boylan-Kolchin et al. 2006; De Lucia & Blaizot 2007). Although major dry mergers are still important for the evolutionary history of BCGs (Bernardi et al. 2011a, b; Brough et al. 2011), the majority of the merging events should have moderate to large mass ratios (Bernardi 2009; Edwards & Patton 2012). Despite this expectation, most studies have focused on the evidence of major mergers in BCGs (Nipoti et al. 2003; Liu et al. 2009). Little attention has been devoted to constraining minor mergers in these systems.

Ever since their discovery (Malin 1979), shell structures have been considered important indicators of merger events in galax-

ies. Shells appear as faint, arc-like stellar structures that are located concentrically within the main body of the galaxy. Observational evidence of their existence has been documented in a number of galaxies (e.g., Schweizer 1980, 1983; Malin & Carter 1980, 1983; Carter 1985; Fort et al. 1986; Forbes & Thomson 1992; Balcells 1997; Canalizo et al. 2007; Sikkema et al. 2007). Most shells are found in galaxies located in low-density environments (Malin & Carter 1983; Colbert et al. 2001). Schweizer (1983) first suggested that shell structures are formed by galaxy mergers. This hypothesis was confirmed through numerical simulations, which showed that shell structures can indeed be produced in minor mergers between an early-type galaxy and a galaxy with much smaller mass (Quinn 1984; Dupraz & Combes 1986; Hernquist & Quinn 1988, 1989; Cooper et al. 2011) and major mergers between equal-mass disk-like galaxies (Hernquist & Spergel 1992). In a minor merger scenario where a massive early-type galaxy and a low-mass galaxy have a nearly radial collision, the stars of the smaller member are stripped off and oscillate around the larger galaxy under the influence of its gravitational potential. Stars with lower binding energy slow down and accumulate at the turning point located at large radii from the center of the main galaxy, followed by the formation of inner shells with higher energy stars. All shells move slowly to larger radii after their formation (e.g., Quinn 1984; Cooper et al. 2011). As their for-

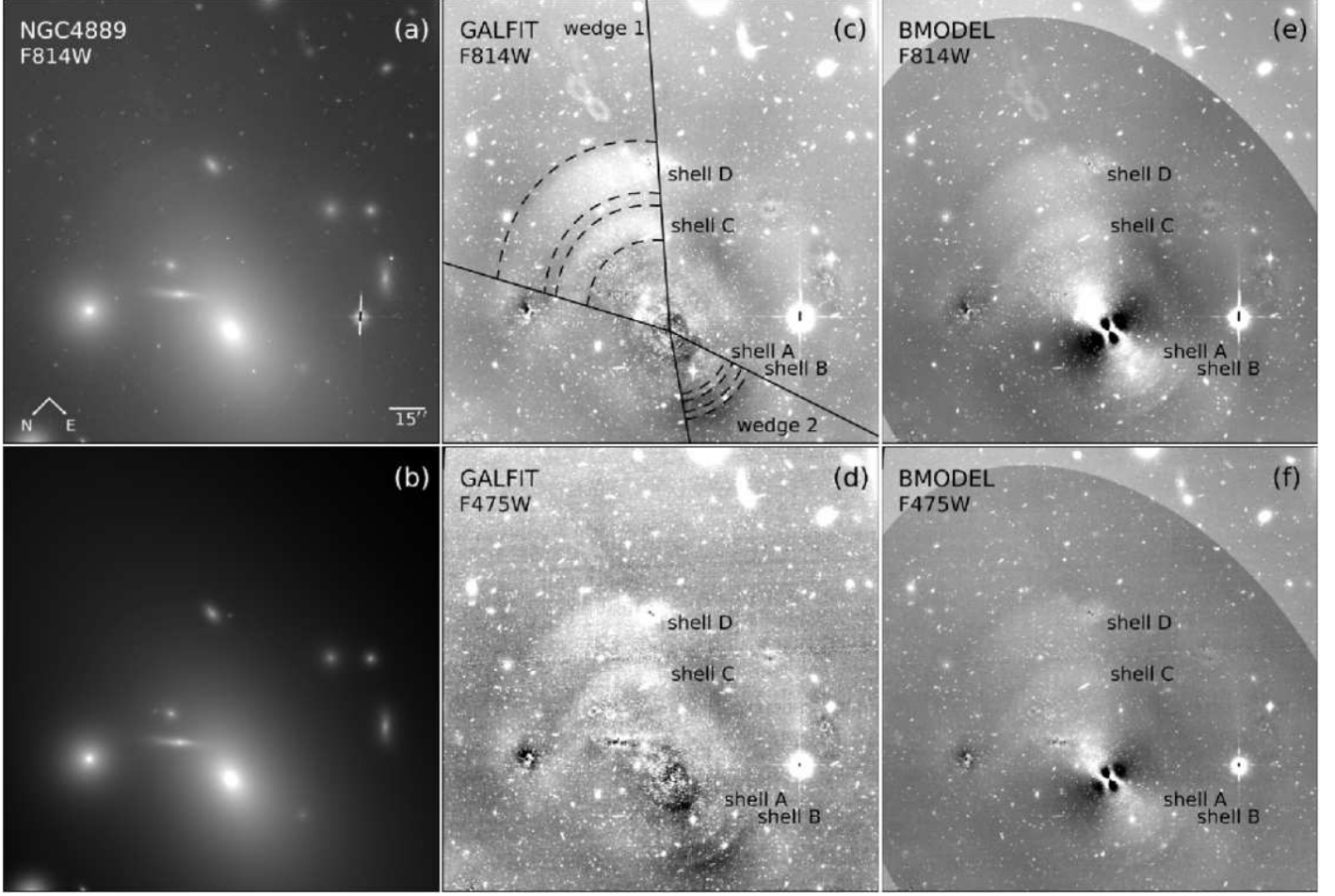


FIG. 2.— Overview of the *HST*/ACS images and the 2-D analysis. (a) F814W image of NGC 4889 and its surrounding galaxies. (b) GALFIT model of the F814W image. (c) Residuals from the GALFIT model of the F814W image; the boundaries of wedge 1 and wedge 2 are labeled, as are the locations of shells A–D. (d) Residuals from the GALFIT model of the F475W image. (e) Residuals from the BMODEL of the F814W image. (f) Residuals from the BMODEL of the F475W image.

mation mechanism is relatively well understood, shells can be used as a tool to diagnose the merger history of massive galaxy.

Shell structures have been rarely studied in BCGs. This paper presents the discovery of shell structures in the Coma cluster BCG NGC 4889. We provide color measurements that allow us to constrain the nature of the merger that produced the shells. We conclude that NGC 4889 experienced a minor merger with a mass ratio of 90 to 1.

The distance of NGC 4889 is assumed to be 100.0 Mpc, adopted from Liu & Graham (2001). Assuming $H_0 = 71 \text{ km s}^{-1} \text{ Mpc}^{-1}$, $\Omega_m = 0.27$, and $\Omega_\Lambda = 0.73$, the distance corresponds to a scale of $0.463 \text{ kpc arcsec}^{-1}$.

2. DATA REDUCTION

Being one of the BCGs in the Coma cluster, NGC 4889 has been observed by various instruments. For the purposes of analyzing the photometric properties of the faint substructures in this massive galaxy, we make use of high-resolution optical images from the Advanced Camera for Surveys (ACS) on the *Hubble Space Telescope* (*HST*) and large field-of-view (FoV) optical images from the Sloan Digital Sky Survey (SDSS) ⁶.

As part of Cycle 17 program 11711 (PI: J. P. Blakeslee), NGC 4889 was observed by *HST*/ACS on March 2010 in both the F475W (pivot wavelength = 4746.9 \AA) and F814W (pivot wavelength = 8057.0 \AA) filters. The ACS/WFC detector contains two CCD chips, each of size 2048×4096 pixels. ACS images provide us high spatial resolution and a moderate FoV ($202'' \times 202''$) of the inner region of NGC 4889. The center of the galaxy is located close to the center of chip 2. The western part of the galaxy is better covered, extending to a radius of 50 kpc. We retrieved two datasets in F475W and one in F814W from the Mikulski Archive for Space Telescopes (MAST) ⁷. The images, pipeline processed by *calasc*, have been flat-fielded, subtracted for dark current and bias level, and corrected for charge transfer efficiency. Each individual dithered image has an exposure time of 730 s in F475W and 830 s in F814W. The total on-source integration time of the final images is 4770 s in F475W and 9960 s in F814W.

The final ACS images in both filters are generated using the DrizzlePac ⁸ task *AstroDrizzle*, which is an enhanced version of *MultiDrizzle* (Koekemoer et al. 2002). This procedure combines the individual dithered images, corrects geometric distortions,

⁶ <http://data.sdss3.org/mosaics>

⁷ <http://archive.stsci.edu/hst/>

⁸ http://www.stsci.edu/hst/HST_overview/drizzlepac

tion, and rejects cosmic rays. During the AstroDrizzle process, sky subtraction is turned on to ensure that each individual frame has the same pedestal when being combined, even though the sky background values of the two final output images are measured later. We use a Gaussian kernel to distribute the flux onto the output images. A series of tests indicates that the Gaussian kernel does the best job at dealing with bad pixels. The output pixel scale is set to $0''.05$. During this procedure, the pixels of the multiple input images are shrunk by a linear factor pixfrac before they are mapped to the output image. The relative weight of each pixel in the output image is recorded in the weight image, which is part of the AstroDrizzle final product. Following the recommendations from the DrizzlePac Handbook (Gonzaga et al. 2012), we use the median value and the standard deviation of the weight image to estimate whether the output image is uniformly covered by the input pixels. To get a decent output image, the selected pixfrac value should allow the standard deviation of the weight image to be less than 20% of the median value. We set the pixfrac value to 0.8 for F475W and 0.6 for F814W, which results in a standard deviation of 17.10% and 11.79% of the median value, respectively, for the central 3000×3000 pixels of the weight images. To ensure that the images are properly aligned, we set the astrometric center and size of the output frames to be the same in the two filters.

We adopted the AB mag system of Oke (1964) and use the updated magnitude zero points for ACS/WFC: 26.056 mag for F475W and 25.947 mag for F814W⁹. The Galactic extinction for NGC 4889 is $A_{\text{F475W}} = 0.031$ mag and $A_{\text{F814W}} = 0.015$ mag (Schlafly & Finkbeiner 2011).

3. MODEL FITTING

We construct model galaxies using GALFIT, a fitting program that uses multiple analytic functions to perform two-dimensional (2-D) decomposition of galaxy images (Peng et al. 2002, 2010). We adopt the Sérsic (1968) function, which has enough flexibility to describe the surface brightness distribution of various types of galaxies. Our primary goal is to detect faint substructures in NGC 4889. To achieve this, we build a monotonically smooth model of the underlying galaxy using as many components as necessary to achieve the best global fit, and then we subtract the best-fit model from the original data to derive a residual image that accentuates low-contrast, low-surface brightness substructure. We ascribe no physical significance to each individual component or to the total number of components. GALFIT normally needs an accurate model of the point-spread function to recover the intrinsic value of the parameters for each model component. To save computation time, we do not account for point-spread function convolution. This has no consequence on our results because we do not attempt to extract physical information from the model parameters. Moreover, the low-surface brightness features we seek are located far from the center of the galaxy; an accurate model for the central regions of the BCG is not necessary for our purposes.

GALFIT uses χ^2 statistics to minimize the difference between the image and the model; hence, the reduced χ^2 value should, in principle, be the natural tool to evaluate the goodness of the fit. However, for large images such as the ones used in our work, it is challenging to assess the robustness of the individual pixel uncertainties required for the calculation of χ^2 . Moreover, the reduced χ^2 is a single parameter that can provide only a very general impression of the quality of the fit. For our

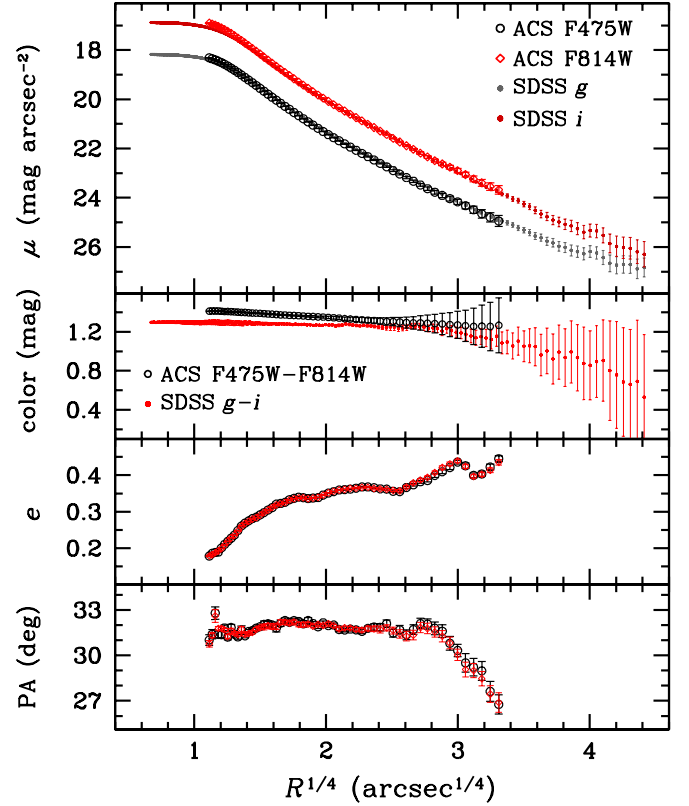


FIG. 3.— 1-D isophotal analysis of *HST*/ACS and SDSS images of NGC 4889. From top to bottom, we show the radial profiles of surface brightness, color, ellipticity, and position angle.

current application, the most straightforward and reliable metric for judging the goodness of the fit is simply from visual inspection of the model-subtracted residual image. The best model is that which achieves the smoothest, flattest residuals using the minimum number of components. This strategy closely resembles that used by Huang et al. (2013) to study the multi-component nature of nearby elliptical galaxies.

We first fit NGC 4889 and its surrounding smaller galaxies with single-component Sérsic models, and then we gradually build up the complexity of the models by adding additional components, if warranted. After each trial, we visually evaluate the quality of the fit and the parameters of the model components. If we encounter any redundant component (one with properties very similar to those of another component) or a component with unreasonable parameters (e.g., very large effective radius, very large ellipticity, or unusually faint central brightness) that does not lead to noticeable improvement in the residual image, we stop the process even though additional components may lead to a lower reduced χ^2 value. Figure 1 illustrates our method, showing two examples of relatively small galaxies near NGC 4889. For the relative simple case in the upper row, a model with two Sérsic components is sufficient because the residual image is already very smooth. On the other hand, the two galaxies on the bottom row require more complicated models to achieve a residual image of the same quality. Six components are needed for the larger galaxy on the left and three for the smaller system on the right.

⁹ <http://www.stsci.edu/hst/acs/analysis/zeropoints/zpt.py>

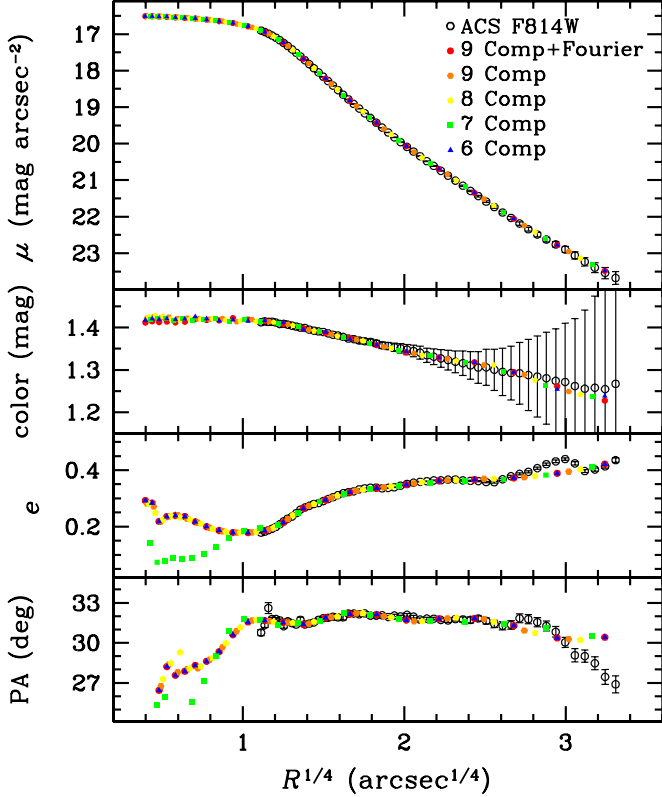


FIG. 4.— 1-D isophotal analysis of the *HST*/ACS F814W image and all GALFIT models of NGC 4889. From top to bottom, we show the radial profiles of surface brightness, color, ellipticity, and position angle. Different models are represented by symbols of different shapes and colors.

3.1. Subtraction of Surrounding Galaxies

As the BCG is embedded in a crowded field (Figure 2), we also need to simultaneously fit and remove all the neighboring galaxies. In total we model 14 small galaxies surrounding NGC 4889. When fitting each of them, we select a rectangular patch covering the target and its nearby region, and mask out irrelevant sources on the patch. The aim is to describe the small galaxies in as much detail as necessary to remove them. We model each galaxy with multiple Sérsic components, enabling Fourier modes (Peng et al. 2010) as needed. There are two disk-like galaxies. To model the smaller one (SDSS J13006.11+275841.9) located to the northeast of NGC 4889, we used nine non-concentric components, adding first, third, and fourth Fourier modes to the seven largest components. For the larger disk galaxy (2MASX J13001036+2757332) located to the west of NGC 4889, we added fourth and sixth Fourier modes to all of its four concentric components. The remaining galaxies were fit well without Fourier modes. The sky background of the neighboring galaxies is the extended envelope of NGC 4889, which has noticeable local curvature due to the BCG. We approximate the background curvature using a large Sérsic component that is centered somewhere outside the image.

We start with the high-signal-to-noise ratio F814W image. Since each small galaxy may affect the model construction of its surrounding counterparts, we adopt the following iterative procedure. We first construct a preliminary model for NGC 4889 and the surrounding galaxies. Then we refit each galaxy using the residual background obtained after subtract-

ing all the other galaxies, thereby producing a refined model for each galaxy. We repeat this procedure until the overall residual pattern is visually satisfactory. Even after we model and subtract the 14 brightest neighbors, the residual images reveal several additional small galaxies projected close to the center of NGC 4889. We do not model these further, and instead simply mask them out during further analysis.

To ensure that we can obtain meaningful color measurements, we must constrain the models constructed from the two filters. The model parameters for the F475W image are tied to those of the F814W image. We fix all the parameters except the absolute positions and integrated magnitudes, to allow slight misalignment and color difference between the two images. The relative positions of the subcomponents in each model are, however, constrained to each other.

3.2. Sky Background Determination

The ACS images do not cover sufficient area to enable a reliable measurement of the sky background, which is essential for our photometric analysis. We estimate the background of the ACS images by scaling the surface brightness profile of the F475W image to that of a wide-field SDSS *g*-band (pivot wavelength = 4770 Å) image over a range of radii unaffected by their resolution difference. The same procedure is used to match the F814W image with the SDSS *i*-band (pivot wavelength = 7625 Å) image. The large-FoV ground-based mosaic images were generated from the Imaging Mosaic tool of SDSS Science Archive Server (SAS). They have already been corrected for the sky by the method described in Blanton et al. (2011); each has a field of $0.65^\circ \times 0.65^\circ$, a pixel scale of $0''.396$, and is centered on NGC 4889.

We use the IRAF¹⁰ task ELLIPSE (Jedrzejewski 1987) to derive one-dimensional (1-D), azimuthally averaged intensity profiles along the semi-major axis of NGC 4889 on the ACS images, after first subtracting the neighboring contaminating galaxies. We apply a mask image that contains three components: (1) the bad pixel map obtained from the weight image as part of the AstroDrizzle output; (2) bright surrounding sources detected by SExtractor (Bertin & Arnouts 1996); and (3), to minimize the effect of the uneven central residual pattern on the isophotal analysis, a manually generated mask for the central region of each surrounding galaxy on the model-subtracted image.

We first run ELLIPSE on the ACS images with fixed central position, which we determined from GALFIT earlier. The ellipticity and position angle are allowed to vary. The radially averaged values of the ellipticity and position angle are then fixed during the next execution of ELLIPSE applied to the mosaic SDSS images. To determine the sky level, we generate an aggressive mask to cover all the bright sources. We median-smooth the images using boxes of different sizes ranging from 3×3 to 55×55 pixels. The unmasked pixel value distribution of each smoothed image is extracted after a 4σ clipping algorithm is iterated for 6 times to reject outliers. We then fit this distribution with a Gaussian function, whose peak gives the expected sky level and the width is taken as the uncertainty. From the relation between the box size for median-smoothing and the uncertainty value, we find that the uncertainty first increases with the box size but remains very stable after 20×20 pixels, which reflects the intrinsic background fluctuation level. In the end,

¹⁰ STSDAS is a product of the Space Telescope Science Institute, which is operated by AURA for NASA

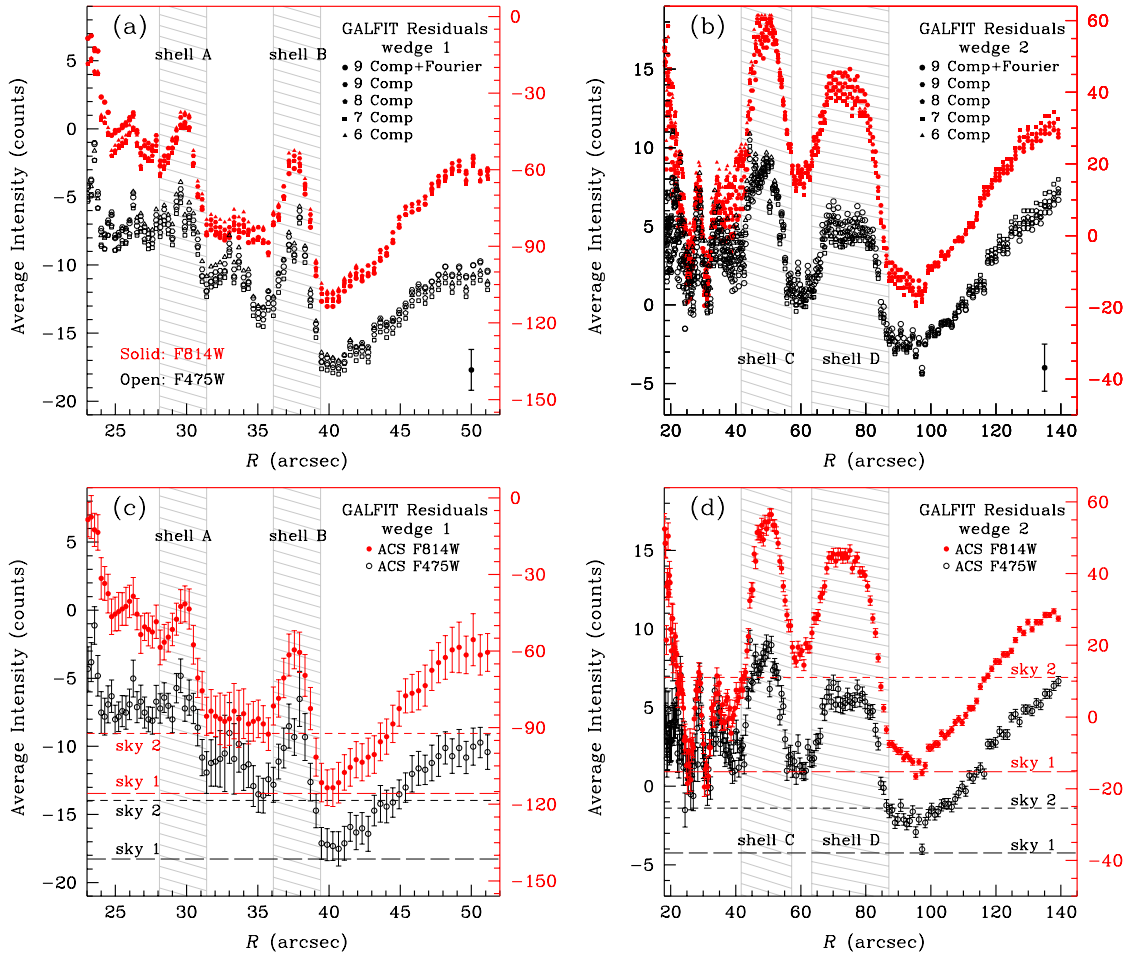


FIG. 5.— Average 1-D intensity profiles of the shell structures generated by subtracting the best GALFIT model from the original images. The shells in each wedge are defined within the radii shaded by the hatched lines. The profiles for the F475W and F814W bands are shown as red (right ordinate) and black dots (left ordinate), respectively. In panels (a) and (b), the results from different models are represented by different symbols. A typical error bar is shown on the lower-right corner. Panels (c) and (d) give the intensity profiles generated from the final, best-fit model, which consists of nine Sérsic components with Fourier modes enabled. The red and black horizontal dashed lines show the level of sky 1 and sky 2 for the F475W and F814W bands, respectively.

we adopt the uncertainty values from images smoothed by a 20×20 box: the value is $(1.50 \pm 12.7) \times 10^{-4}$ counts s^{-1} for g and $(8.3 \pm 33.0) \times 10^{-4}$ counts s^{-1} for i .

Next, we derive the g -band and i -band surface brightness profiles of the SDSS images, after applying object masks generated from SExtractor. The ellipticity and position angle are fixed to the values determined from the ACS images. Because of the coarse resolution of the SDSS images, a larger step size (0.05 compared with 0.02) is adopted for incrementing the factor by which the semi-axis length is increased between successive isophotes. We estimate the background level of the ACS images by matching the F475W and g profiles and the F814W and i profiles (Figure 3). We neglect the central $3''$ region to avoid the obvious mismatch between the *HST* and SDSS point-spread functions. On larger scales the comparison can only be made out to $\sim 115''$ because the ACS images have a more limited FoV compared with the SDSS. We use a non-linear least-squares optimization method to join up the brightness profiles. During the fitting procedure, two variables are optimized simultaneously. The first variable is the sky background value of the ACS images. The second variable is a constant offset in the overall photometric zero point that practically accounts for the difference in photometric zero point between the ACS and its corresponding SDSS filter.

The intrinsic fluctuation of the background level of the ACS images is an important factor that affects the uncertainty on the sky. We first explain here the procedure for measuring the intrinsic fluctuation of the background and defer the discussion on model construction and shell detection for the next section. We measure the intrinsic fluctuation on the GALFIT residual images after subtracting the surrounding galaxies and the model for NGC 4889 from the original data. We apply the mask used in constructing the GALFIT models to exclude all the bright sources and faint shell structures. Then we apply a procedure similar to that used for the SDSS images: we median-smooth the images using boxes of different sizes, ranging from 3×3 to 55×55 pixels, and we apply a 4σ clipping algorithm 6 times to reject outliers on the smoothed images. A Gaussian function is then fit to the unmasked pixel; the width of the distribution is taken as the uncertainty. Adopting, as before, the images smoothed by a 20×20 box, the intrinsic fluctuations are 1.326×10^{-3} counts s^{-1} for the F475W image and 3.002×10^{-3} counts s^{-1} for the F814W image. The final uncertainty of the sky level of the ACS images is the combination of the sky uncertainty of the SDSS images, the uncertainty from the least-squares optimization method, and the intrinsic fluctuation of the ACS images.

TABLE 1 : MODEL-INDEPENDENT PARAMETERS FOR THE SHELLS

Name	Direction	Location		Thickness		Length	e	PA
		(")	(kpc)	(")	(kpc)	($^{\circ}$)		($^{\circ}$)
shell A	SW	29.8	13.8	3.3	1.5	53	0.07	23
shell B	SW	37.8	17.5	3.3	1.5	53	0.07	23
shell C	NE	49.7	23.0	15.9	7.4	69	0.19	30
shell D	NE	75.3	34.9	23.7	11.0	69	0.19	30

NOTE.— Column 1: shell name. Column 2: direction of each shell respect to NGC 4889. Column 3 and 4: location of each shell respect to the center of NGC 4889. Column 5 and 6: thickness of each shell. Column 7, 8 and 9: length, ellipticity and position angle of each shell measured on the elliptical annuli enclosing it.

3.3. Detection of Shell Features in NGC 4889

Shells, as low-surface brightness features, are difficult to detect and measure in the presence of their bright host galaxies. To reveal the photometric properties of shell structures, we use the residual images made by subtracting the model of the host galaxy. Because shells are very faint, even small deviations in the host galaxy model can greatly affect the inferred light distribution of the shell structures on residual images. The photometric properties of shell structures are therefore strongly model-dependent. We require an accurate and carefully constructed model for the host galaxy. We build a host galaxy model two ways, first by using GALFIT and then independently verifying it using a non-parametric approach based on isophotal analysis. In both cases we first subtract the surrounding small galaxies from the images.

We built five different host galaxy models using GALFIT. Each model consists of three to nine Sérsic components and a sky component. During the fitting we apply a mask generated from the combination of the mask used for ELLIPSE plus an additional one that covers all the shell regions. With the shell regions masked out, we are able to build models that describe only the host galaxy without the influence of the shell structures. The average sky background is fixed to the value derived in Section 3.2. In view of possible variations in the local background due to the nearby galaxies or intracluster light, we further allow the sky gradient to be adjusted. The fits are first performed on the deeper F814W image, with all the parameters for each Sérsic component free to vary. Most of the resulting parameters are then used and fixed in the F475W model, including the effective radius, Sérsic index, ellipticity, and position angle. Only the integrated magnitude of each component is allowed to vary. Models generated in F475W and F814W have exactly the same size and shape.

An initial three-component fit of NGC 4889 suffices to reveal the presence of shell structures, but strong features remain in the residual images. Six components give a much flatter residual pattern, but the innermost part of the galaxy, mostly within 200 pixels from the center, is still not well fit. We gradually increased the number of components, one at a time, eventually finding the optimal solution to be nine components with the 4th and 6th Fourier modes turned on for the six innermost components. The middle panels of Figure 2 give the residual images from our final, best-fit nine-component model with Fourier modes enabled. For completeness, however, we illustrate the other four acceptable models (Figure 4). All show satisfactory 2-D residual patterns and rather similar 1-D surface brightness, ellipticity, and position angle profiles.

We use a non-parametric approach to independently confirm

the reality of the shell structures and that they are not artifacts generated by our parametric fits. We use the IRAF task BMODEL to construct a smooth model of NGC 4889 using the best-fitting isophotes generated from the 1-D analysis using ELLIPSE. We manually correct the sky background using the sky level found in Section 3.2, and we run ELLIPSE with the ellipticity and position angle fixed to the values derived in the previous section. To trace the galaxy smoothly and with the best fidelity, we set the fitting step to 0.05 and compute the median rather than the mean intensity. The BMODEL residual images are shown on the right column of Figure 2. It is reassuring that the overall shell features are robust substructures: their general appearance is very similar in the GALFIT and BMODEL residual images.

Despite the overall similarity of both methods in revealing the presence of shells, we advocate that the GALFIT-based 2-D method as the better choice for quantitative analysis of the shell features, for the following reasons. The GALFIT approach allows us to construct consistent, well-constrained models for images taken in different filters (e.g., by coupling the geometric parameters of the various subcomponents). This is absolutely crucial to derive robust colors for the shell features. Moreover, GALFIT has better ability to handle images that have been aggressively masked, as is necessary for the very complicated environment surrounding NGC 4889 and other BCGs. By contrast, ELLIPSE and other isophote fitting routines will often fail when confronted with such large regions of flagged pixels. GALFIT uses the information in the entire 2-D image, while ELLIPSE fits each isophote using only the information around a pre-defined semi-major axis length. Even small local irregularities in the image that are not perfectly masked can influence the mean intensity of the corresponding elliptical isophote. A 2-D reconstruction of the isophotes using BMODEL produces ring-like structures in the residual images that can be mistaken for real shell features.

4. LOCATION AND COLOR OF THE SHELLS

Four shells are unambiguously detected in the residual images generated from both the GALFIT and BMODEL models. We highlight the shells with dashed lines on Figure 2. Ordered according to their distance from the center of NGC 4889, they are marked as shells A (13.8 kpc), B (17.5 kpc), C (23.0 kpc), and D (34.9 kpc). Shells A and B are located to the northeast of the galaxy, and shells C and D are located on the southwestern side. At first glance, all the shells are roughly aligned with the major axis of the host galaxy. The position angle is 23° for shells A and B and 30° for shells C and D, to be compared with a position angle of 31° for the host galaxy. The inner two shells are much thinner ($3''.3$) and shorter ($53''$) than the outer

TABLE 2 : MAGNITUDES AND COLORS OF THE SHELLS

Model	F475W-F814W (sky 1)	F475W-F814W (sky 2)	F814W (sky 1)	F814W (sky 2)	F475W-F814W (NGC 4889)
(1)	(2)	(3)	(4)	(5)	(6)
shell A					
9 Sérsic+Fourier	1.132 ± 0.007	1.128 ± 0.012	20.127 ± 0.005	20.663 ± 0.008	1.302 ± 0.002
9 Sérsic	1.115 ± 0.007	1.095 ± 0.012	20.137 ± 0.005	20.697 ± 0.008	
8 Sérsic	1.142 ± 0.007	1.124 ± 0.012	20.105 ± 0.005	20.606 ± 0.008	
7 Sérsic	1.129 ± 0.007	1.110 ± 0.012	20.112 ± 0.005	20.604 ± 0.008	
6 Sérsic	1.124 ± 0.007	1.106 ± 0.012	20.084 ± 0.004	20.602 ± 0.008	
shell B					
9 Sérsic+Fourier	1.093 ± 0.010	1.023 ± 0.028	20.416 ± 0.007	21.454 ± 0.019	1.292 ± 0.002
9 Sérsic	1.103 ± 0.010	1.041 ± 0.028	20.393 ± 0.007	21.436 ± 0.019	
8 Sérsic	1.177 ± 0.010	1.182 ± 0.022	20.294 ± 0.006	21.116 ± 0.014	
7 Sérsic	1.181 ± 0.010	1.199 ± 0.022	20.293 ± 0.006	21.090 ± 0.014	
6 Sérsic	1.174 ± 0.010	1.197 ± 0.023	20.282 ± 0.006	21.153 ± 0.015	
shell C					
9 Sérsic+Fourier	1.152 ± 0.002	0.829 ± 0.006	17.730 ± 0.002	18.407 ± 0.004	1.285 ± 0.002
9 Sérsic	1.191 ± 0.002	0.878 ± 0.005	17.649 ± 0.002	18.293 ± 0.004	
8 Sérsic	1.228 ± 0.002	0.957 ± 0.005	17.605 ± 0.002	18.156 ± 0.003	
7 Sérsic	1.264 ± 0.002	0.971 ± 0.005	17.596 ± 0.002	18.143 ± 0.003	
6 Sérsic	1.213 ± 0.002	0.954 ± 0.005	17.589 ± 0.002	18.133 ± 0.003	
shell D					
9 Sérsic+Fourier	1.181 ± 0.002	0.788 ± 0.007	16.975 ± 0.002	17.799 ± 0.005	1.260 ± 0.002
9 Sérsic	1.197 ± 0.002	0.744 ± 0.007	16.987 ± 0.002	17.874 ± 0.006	
8 Sérsic	1.212 ± 0.002	0.772 ± 0.007	17.021 ± 0.002	17.849 ± 0.006	
7 Sérsic	1.231 ± 0.002	0.735 ± 0.007	17.034 ± 0.002	17.882 ± 0.006	
6 Sérsic	1.207 ± 0.002	0.779 ± 0.007	17.022 ± 0.002	17.858 ± 0.006	

NOTE.— Column 1: Index of GALFIT model. Column 2 and 3: F475W-F814W colors of the shells and their photometric uncertainties using sky 1 and sky 2. Column 4 and 5: Integrated apparent F814W magnitudes of the shells and their photometric uncertainties using sky 1 and sky 2. Column 6: F475W-F814W color of the host galaxy, NGC 4889, at the location of each shell and corresponding photometric uncertainty. Magnitudes and colors are corrected for Galactic extinction.

two shells ($15''.9$ and 69° for shell C; $23''.7$ and 69° for shell D). By comparing the residual images generated using the two methods, it is obvious that GALFIT gives a more distinct view of the shell structures. The residuals from BMODEL have fan-like artifacts that are not present in the GALFIT residuals.

We first need to define the physical boundaries of the shells in order to be able to measure their photometric properties. We obtain the basic geometric parameters for the four shells by visually drawing elliptical annuli that approximately enclose the shell-like brightness enhancements visible on the F814W residual image. Table 1 lists the derived radii, thickness, length, ellipticity, and position angle of the shells. Based on the geometric information of the shells, we establish two wedge-shaped regions to enclose them, as shown on Figure 2c. Wedge 1 encloses shells A and B; Wedge 2 contains shells C and D. We then use ELLIPSE to calculate the average intensity profile of each shell within the wedges. The center of the fitted isophotes are all fixed at the center of NGC 4889, and the ellipticity and position angle are fixed to the values determined for each shell.

Figures 5a and 5b show the average intensity profiles for the shells. Results from the different GALFIT models are given. While the intensity profile is very complex, we can clearly identify four peaks that correspond to the four shells seen in the 2-D residual images. The location of the peaks are marked with light shaded regions. Overall there is good agreement among the different models. The basic shapes of the shell profiles are robust, and the main differences come from slight offsets in the normalization of the intensity. There is also good correspondence between the two filters. Even though the F475W data set

is noisier, it clearly traces the same overall structures seen more clearly in the F814W image.

We perform aperture photometry on the GALFIT residual images to determine the integrated apparent magnitude and color of the shells, using apertures defined using the geometric parameters established above. Although the ACS images have had their global sky background subtracted, as described in Section 3.2, we need to redetermine the *local* background for each shell in order to properly measure its brightness because it sits on top of significant diffuse emission that presumably belongs to real signal from NGC 4889 and/or intracluster light. We illustrate our approach in Figure 5c and 5d, using, as an example, the 1-D average intensity profiles generated from the best-fitting nine-component Sérsic model with Fourier modes. Within each wedge and for each shell, we define the local background to be one of the two low-intensity regions determined from the 1-D profiles. Within each wedge, “sky 1” is located beyond the two shells, while “sky 2” is located between the two shells. The sky regions have the same range in radius, ellipticity, and position angle as those of shells within the wedge. Their inner and outer radii are carefully estimated by visual inspection of the 1-D profiles, to ensure that they enclose all the low-intensity pixels. Within each sky region, we measure the sky value using the same method employed for measuring the sky on large scales (Section 3.2). Namely, (1) we mask out any remaining bright sources; (2) we apply six iterations of 4σ clipping; and (3) we fit a Gaussian to the distribution of sky pixel values and then adopt the peak of the Gaussian as the local sky level and the width of the Gaussian as the error on the sky. Note

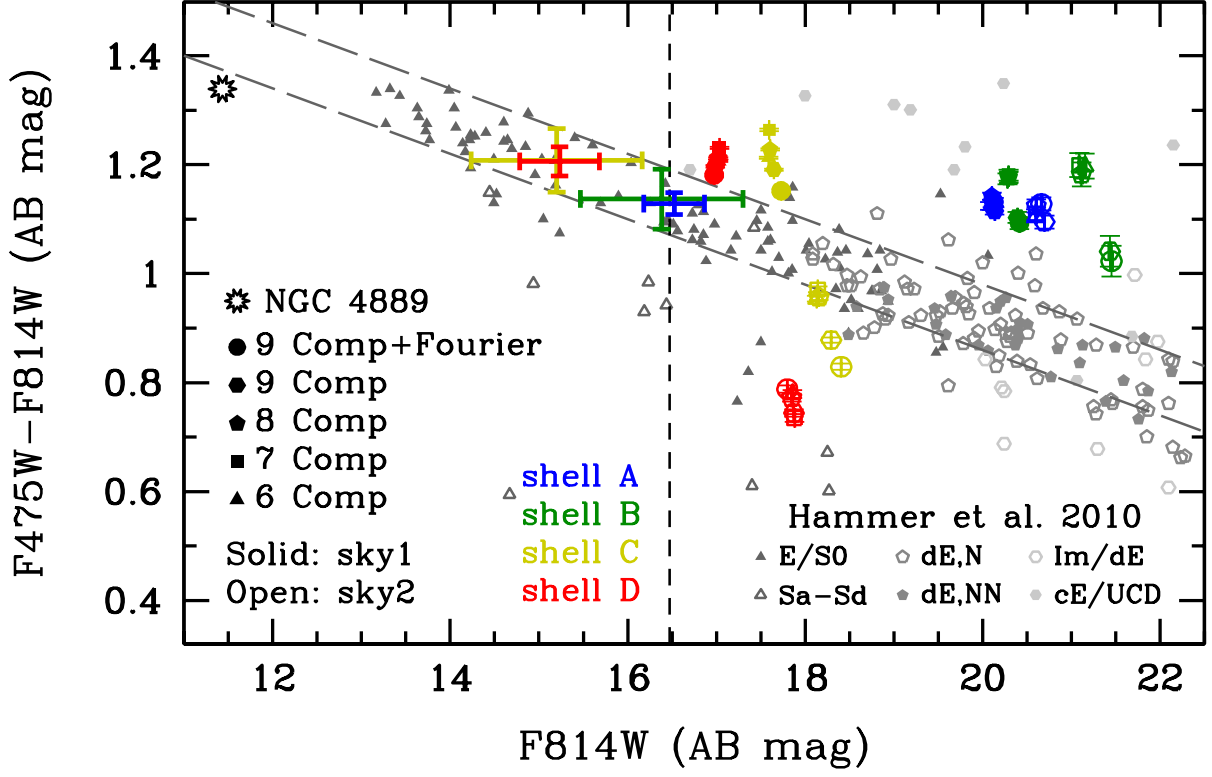


FIG. 6.— The CMR of Coma cluster galaxies as given by Hammer et al. (2010; diagonal long-dashed lines). The gray points represent data from Hammer et al. (2010). Different galaxy types are marked by different symbols and slightly different shades of gray. The measured magnitudes and colors of the four shells are shown in blue, green, yellow, and red symbols, with the different models denoted by various symbol types. The magnitude of each shell predicted from the CMR is plotted as error bars in the corresponding color. NGC 4889 is plotted as a black star. The vertical dashed line marks the total magnitude of the four shells.

that, because of sigma-clipping, the actual values of sky 1 and sky 2 are slightly lower than the corresponding values inferred from the minima of the 1-D profiles.

The integrated apparent magnitude of each shell is calculated using the following formulae:

$$mag = zmag - 2.5 \log \left(\frac{flux - A \times sky}{t_{exp}} \right) \quad (1)$$

$$\sigma_{mag} = 1.0857 \frac{\sigma}{flux - A \times sky}. \quad (2)$$

In the above equations, $zmag$ (mag) is the photometric zero point for the respective filter, $flux$ (counts) is the total flux within the aperture, with associated error σ , A is the number of pixels in the aperture, sky (counts/pixel) is the sky level, and t_{exp} (seconds) is the exposure time. We use both sky 1 and sky 2 for the sky level. We calculate σ using

$$\sigma = \sqrt{\frac{flux - A \times sky}{gain} + A \times \sigma_{sky}^2 + \frac{A^2 \times \sigma_{sky}^2}{A_{sky}}}. \quad (3)$$

Here, gain (e-/ADU) is the gain value of the detector. Because of their low surface brightnesses, the final magnitudes and especially the colors are highly model-dependent. The measurements are sensitive not only to the global GALFIT model adopted, but also to the choice of local sky background. The measurements for all five GALFIT models and using both prescriptions for local sky determination are presented in Table 2 and illustrated in Figure 6. These measurements bracket the full range of possible systematic uncertainties. We believe that the

most robust measurements come from the nine-component Sérsic model with Fourier modes combined with the local background estimated using sky 1. The apparent magnitude of all four shells combined is $m_{F814W} = 16.453 \pm 0.018$; it is marked by the vertical dashed line on Figure 6. The colors for shells A and B are quite similar for sky 1 and sky 2, but they differ significantly for shells C and D. Adopting sky 1 as the fiducial background, the color of shells A–D are $F475W-F814W = 1.129 \pm 0.021$, 1.137 ± 0.055 , 1.208 ± 0.058 , and 1.206 ± 0.027 , respectively. The shells have colors in the range $F475W-F814W \approx 1.1-1.2$ mag. The shell colors are significantly bluer than the integrated color of NGC 4889, which is $F475W-F814W = 1.34$ mag within an aperture with a semi-major axis length of $40''$, similar to that adopted by Carter et al. (2009). Moreover, each shell is slightly, but measurably *bluer* than the color of NGC 4889 at the location of each shell, which lies in the range $F475W-F814W \approx 1.26-1.30$ mag. This represents one of the very few robust color measurements of shells in BCGs, and the first to show unambiguously that the shells have different colors than the underlying host galaxy.

5. PHYSICAL IMPLICATIONS

Minor mergers, especially those that involve little or no dissipation, are now frequently invoked to explain the mass and size evolution of massive early-type galaxies. The accretion of smaller stellar systems without significant cold gas can help build up the extended envelopes of massive ellipticals. The shell structures we found in NGC 4889 can be regarded as an evidence of the type of minor merger event envisioned. The location of NGC 4889 in Coma suggests that the shells were

probably not generated through gas-rich or major mergers: the probability of either is low in the core of a rich cluster. Instead, the shells were most likely formed from a minor merger (Quinn 1984; Dupraz & Combes 1986; Hernquist & Quinn 1988, 1989; Cooper et al. 2011). Furthermore, the lack of dust lanes or other substructures in the residual images of NGC 4889 that might indicate the presence of cold gas strongly hints that the minor merger event was dry.

Beyond their mere discovery, the shells in NGC 4889 can be used to deduce a quantitative estimate of the mass of the accreted galaxy. The key lies in the colors of the shells.

Early-type galaxies in clusters obey an extraordinary tight color-magnitude relation (CMR): more luminous galaxies are redder (Faber 1973; Visvanathan & Sandage 1977). Although broad-band optical colors are notoriously difficult to interpret because of the degeneracy among age, metallicity, and dust reddening, the situation is considerably cleaner for early-type galaxies, especially those in clusters, which, to zeroth order, are old and dust-free. The CMR for early-type galaxies is widely viewed as a correlation between metallicity and luminosity or stellar mass (Faber 1973; Larson 1975; Kodama & Arimoto 1997).

The Coma cluster, in particular, exhibits a well-developed, tight CMR covering a wide range of galaxy types and luminosities (e.g., Dressler 1980; Godwin et al. 1983; Bower et al. 1992; Terlevich et al. 1999, 2001). The recent measurements from the *HST*/ACS Coma Cluster Survey (Hammer et al. 2010) are especially useful for our purposes because it used exactly the same filter pair we used. Hammer et al. (2010; their Figure 13) constructed a deep CMR for Coma that extends down to about 22.0 AB magnitude in the F814W filter. Their sample is reproduced in Figure 6, where we now add our measurements of the four shells in NGC 4889 and the integrated quantities for NGC 4889 itself. Each shell is coded by a different color, and the results for the different GALFIT models are shown with different symbols. Focusing only on the measurements using sky 1, the color of shells A–D are $F475W - F814W = 1.129 \pm 0.021$, 1.137 ± 0.055 , 1.208 ± 0.058 , and 1.206 ± 0.027 , respectively, where the error bar represents the dispersion among the five models. The diagonal long-dashed lines bracket the scatter of Hammer et al.’s fit to the CMR for Coma:

$$F475W - F814W = -0.06 \times F814W + 2.12. \quad (4)$$

It is immediately clear that the shells lie significantly and systematically *above* the CMR. The individual shells are “too red” for their luminosities. This is true for all of the shells if the colors are derived using sky 1 as the background, and it is true of shells A and B even if we assumed sky 2. As explained in Section 4, we think that sky 1 is more trustworthy than sky 2, and for the rest of the paper we will focus only on measurements made using sky 1.

We can naturally explain the anomalous position of the shells under the hypothesis that the shells represent the trace remnants of a once-disrupted larger galaxy. The shells bear the imprint of the metallicity (or color) of their progenitor galaxy, *before* it fell into NGC 4889 and was torn apart. We assume, reasonably, that the progenitor was a member of Coma and that it used to follow the CMR of the cluster. We further assume that all four shells were formed in a single merger event, and that on average the colors of the shells are similar to the color of the progenitor galaxy. By extrapolating the observed colors of the shells back to the CMR, we can constrain the original luminosity (or mass)

of the progenitor galaxy.

The large colored error bars show the predicted locations of the progenitor on the CMR. The magnitudes range from as bright as $F814W = 15.17$ for shells C and D to as faint as 16.50 for shell A. For an integrated magnitude of $F814W = 11.44$ for NGC 4889, measured within the same $40''$ aperture used to obtain its colors, the range of possible progenitor luminosity (mass) ratios (with respect to NGC 4889) is 31:1 to 106:1. According to numerical simulations (e.g., Quinn 1984), the innermost shells form last. We thus expect the inner shells to better reflect the actual properties of the progenitor galaxy as they should be less contaminated by mixing with the ambient stars. Within our data set, the colors of the two inner shells have the additional advantage of being better measured than those for the two outer ones. Shell B, in particular, is relatively isolated and has the best determined local background (see Figure 5). With $F475W - F814W = 1.137 \pm 0.055$ mag, the CMR predicts $F814W = 16.33$ mag for the progenitor, which corresponds to a luminosity (mass) ratio of 90:1. The observed total magnitude of the four shells, $F814W = 16.453 \pm 0.018$, yields a firm lower limit to the luminosity (mass) ratio of $\sim 100:1$. Interestingly, our best estimate for the luminosity of the progenitor (based on the color of shell B) agrees remarkably well with the combined luminosity of the four shells. This implies that most of the mass of the disrupted satellite actually ended up in the four shells that we detected.

What is the nature of the shell progenitor? Adopting the results based on our analysis of shell B, the disrupted galaxy had an absolute *I*-band magnitude of -18.7 . This luminosity suggests that the progenitor was brighter than a typical dwarf galaxy. Considering the unique location of NGC 4889 in the cluster core and the types of galaxies that currently surround it, it is reasonable to assume that the progenitor was an early-type system. Moreover, numerical simulations suggest that the formation of regular shell structures normally requires the progenitor to have a relatively low stellar velocity dispersion. Putting all of these clues together, we propose that the progenitor was most likely a sizable disk galaxy, presumably a low-mass S0 or early-type spiral.

6. SUMMARY

We have discovered a system of four stellar shell features in NGC 4889, the BCG in the Coma cluster. The shells are well aligned with the major axis of the host galaxy. The unique environment of NGC 4889 in the central region of the massive Coma cluster, combined with the non-detection of any dust features, suggests that the shells are structures formed through a non-dissipative merger event. We present a detailed 2-D structural decomposition of *HST*/ACS images of the BCG and its complex surroundings, including a careful determination of the global and local sky background with the help of large-field images from SDSS. These technical steps are crucial for securing an accurate determination of the photometric properties of the shells. We have successfully measured not only the luminosities but also the colors of the shells. The shells are found to be slightly bluer than the host galaxy at the same location.

Under the assumption that the shells were created by a small satellite galaxy that fell into NGC 4889, and that the progenitor system obeyed the present-day observed color-magnitude relation of the Coma cluster, we use the measured colors of the shells to infer the luminosity (mass) of the disrupted galaxy. We estimate that the shell progenitor galaxy had an *I*-band

absolute magnitude of -18.7 , roughly 90 times less luminous than NGC 4889. The combined luminosity of the four shells is roughly consistent with the progenitor luminosity inferred from our analysis of the CMR, which suggests that most of the mass of the disrupted galaxy remained in the shell structures.

The techniques outlined in this study provide a novel strategy to use the photometric substructure of early-type galaxies to constrain the mass ratio and other useful physical properties of past minor merger events.

This work was supported by the Carnegie Institution for Science (LCH) and the China Scholarship Council (MG, SH), and under the National Natural Science Foundation of China under grant 11133001 and 11273015 (MG, SH). MG and SH thank

Prof. Q.-S. Gu and the School of Astronomy and Space Science of Nanjing University for providing long-term support. Funding for the SDSS and SDSS-II has been provided by the Alfred P. Sloan Foundation, the Participating Institutions, the National Science Foundation, the U.S. Department of Energy, the National Aeronautics and Space Administration, the Japanese Monbukagakusho, the Max Planck Society, and the Higher Education Funding Council for England. The SDSS Web site is <http://www.sdss.org>. This research has made use of the NASA/IPAC Extragalactic Database (NED) which is operated by the Jet Propulsion Laboratory, California Institute of Technology, under contract with the National Aeronautics and Space Administration. We thank the anonymous referee for helpful comments that improved this paper.

REFERENCES

- Balcells, M. 1997, *ApJ*, 486, L87
 Bezanson, R., van Dokkum, P. G., Tal, T., et al. 2009, *ApJ*, 697, 1290
 Bernardi, M. 2009, *MNRAS*, 395, 1491
 Bernardi, M., Roche, N., Shankar, F., & Sheth, R. K. 2011a, *MNRAS*, 412, 684
 Bernardi, M., Roche, N., Shankar, F., & Sheth, R. K. 2011b, *MNRAS*, 412, L6
 Bertin, E., & Arnouts, S. 1996, *A&AS*, 117, 393
 Blanton, M. R., Kazin, E., Muna, D., Weaver, B. A., & Price-Whelan, A. 2011, *AJ*, 142, 31
 Bower, R. G., Lucey, J. R., & Ellis, R. S. 1992, *MNRAS*, 254, 589
 Boylan-Kolchin, M., Ma, C.-P., & Quataert, E. 2006, *MNRAS*, 369, 1081
 Brough, S., Tran, K.-V., Sharp, R. G., von der Linden, A., & Couch, W. J. 2011, *MNRAS*, 414, L80
 Canalizo, G., Bennert, N., Jungwiert, B., et al. 2007, *ApJ*, 669, 801
 Cappellari, M., di Serego Alighieri, S., Cimatti, A., et al. 2009, *ApJ*, 704, L34
 Carter, D. 1985, *Lecture Notes in Physics: New Aspects of Galaxy Photometry* (Berlin:Springer-Verlag, 215
 Carter, D., Smith, D. J. B., Percival, S. M., et al. 2009, *MNRAS*, 397, 695
 Cimatti, A., Daddi, E., Renzini, A., et al. 2004, *Nature*, 430, 184
 Cocato, L., Gerhard, O., & Arnaboldi, M. 2010, *MNRAS*, 407, L26
 Colbert, J. W., Mulchaey, J. S., & Zabludoff, A. I. 2001, *AJ*, 121, 808
 Cooper, A. P., Martínez-Delgado, D., Helly, J., et al. 2011, *ApJ*, 743, L21
 Daddi, E., Renzini, A., Pirzkal, N., et al. 2005, *ApJ*, 626, 680
 Damjanov, I., Abraham, R. G., Glazebrook, K., et al. 2011, *ApJ*, 739, L44
 Dekel, A., Sari, R., & Ceverino, D. 2009, *ApJ*, 703, 785
 De Lucia, G., & Blaizot, J. 2007, *MNRAS*, 375, 2
 Dressler, A. 1980, *ApJS*, 42, 565
 Dubinski, J. 1998, *ApJ*, 502, 141
 Dupraz, C., & Combes, F. 1986, *A&A*, 166, 53
 Edwards, L. O. V., & Patton, D. R. 2012, *MNRAS*, 425, 287
 Faber, S. M. 1973, *ApJ*, 179, 731
 Fabian, A. C. 1994, *ARA&A*, 32, 277
 Forbes, D. A., & Thomson, R. C. 1992, *MNRAS*, 254, 723
 Fort, B. P., Prieur, J.-L., Carter, D., Meatheringham, S. J., & Vigroux, L. 1986, *ApJ*, 306, 110
 Godwin, J. G., Metcalfe, N., & Peach, J. V. 1983, *MNRAS*, 202, 113
 Gonzaga, S., Hack, W., Fruchter, A., Mack, J., eds. 2012, *The DrizzlePac Handbook* (Baltimore: STScI)
 Greene, J. E., Murphy, J. D., Comerford, J. M., Gebhardt, K., & Adams, J. J. 2012, *ApJ*, 750, 32
 Hammer, D., Verdoes Kleijn, G., Hoyos, C., et al. 2010, *ApJS*, 191, 143
 Hernquist, L., & Quinn, P. J. 1988, *ApJ*, 331, 682
 Hernquist, L., & Quinn, P. J. 1989, *ApJ*, 342, 1
 Hernquist, L., & Spergel, D. N. 1992, *ApJ*, 399, L117
 Huang, S., Ho, L. C., Peng, C. Y., Li, Z.-Y., & Barth, A. J. 2013, *ApJ*, 766, 47
 Jedrzejewski, R. I. 1987, *MNRAS*, 226, 747
 Khochfar, S., & Silk, J. 2006, *MNRAS*, 370, 902
 Kodama, T., & Arimoto, N. 1997, *A&A*, 320, 41
 Koekemoer, A. M., Fruchter, A. S., Hook, R. N., & Hack, W. 2002, in *HST Calibration Workshop*, ed. S. Arribas, A. M. Koekemoer, & B. Whitmore (Baltimore: STScI), 337
 Lackner, C. N., Cen, R., Ostriker, J. P., & Joung, M. R. 2012, *MNRAS*, 425, 641
 Larson, R. B. 1975, *MNRAS*, 173, 671
 Liu, F. S., Mao, S., Deng, Z. G., Xia, X. Y., & Wen, Z. L. 2009, *MNRAS*, 396, 2003
 Liu, M. C., & Graham, J. R. 2001, *ApJ*, 557, L31
 Malin, D. F. 1979, *Nature*, 277, 279
 Malin, D. F., & Carter, D. 1980, *Nature*, 285, 643
 Malin, D. F., & Carter, D. 1983, *ApJ*, 274, 534
 Merritt, D. 1985, *ApJ*, 289, 18
 Naab, T., Johansson, P. H., & Ostriker, J. P. 2009, *ApJ*, 699, L178
 Naab, T., Khochfar, S., & Burkert, A. 2006, *ApJ*, 636, L81
 Nipoti, C., Stiavelli, M., Ciotti, L., Treu, T., & Rosati, P. 2003, *MNRAS*, 344, 748
 Oke, J. B. 1964, *ApJ*, 140, 689
 Onodera, M., Renzini, A., Carollo, M., et al. 2012, *ApJ*, 755, 26
 Oser, L., Naab, T., Ostriker, J. P., & Johansson, P. H. 2012, *ApJ*, 744, 63
 Oser, L., Ostriker, J. P., Naab, T., Johansson, P. H., & Burkert, A. 2010, *ApJ*, 725, 2312
 Ostriker, J. P., & Hausman, M. A. 1977, *ApJ*, 217, L125
 Ostriker, J. P., & Tremaine, S. D. 1975, *ApJ*, 202, L113
 Peng, C. Y., Ho, L. C., Impey, C. D., & Rix, H.-W. 2002, *AJ*, 124, 266
 Peng, C. Y., Ho, L. C., Impey, C. D., & Rix, H.-W. 2010, *AJ*, 139, 2097
 Postman, M., & Lauer, T. R. 1995, *ApJ*, 440, 28
 Quinn, P. J. 1984, *ApJ*, 279, 596
 Sandage, A. 1976, *ApJ*, 205, 6
 Schlafly, E. F., & Finkbeiner, D. P. 2011, *ApJ*, 737, 103
 Schweizer, F. 1980, *ApJ*, 237, 303
 Schweizer, F. 1983, in *IAU Symp. 100, Internal Kinematics and Dynamics of Galaxies* (Dordrecht: Reidel), 319
 Sérsic, J. L. 1968, *Atlas de Galaxias Australes* (Córdoba: Obs. Astron., Univ. Nac. Córdoba)
 Sikkema, G., Carter, D., Peletier, R. F., et al. 2007, *A&A*, 467, 1011
 Silk, J. 1976, *ApJ*, 208, 646
 Szomoru, D., Franx, M., & van Dokkum, P. G. 2012, *ApJ*, 749, 121
 Terlevich, A. I., Caldwell, N., & Bower, R. G. 2001, *MNRAS*, 326, 1547
 Terlevich, A. I., Kuntschner, H., Bower, R. G., Caldwell, N., & Sharples, R. M. 1999, *MNRAS*, 310, 445
 Toomre, A., & Toomre, J. 1972, *ApJ*, 178, 623
 Trujillo, I., Conselice, C. J., Bundy, K., et al. 2007, *MNRAS*, 382, 109
 Trujillo, I., Feulner, G., Goranova, Y., et al. 2006, *MNRAS*, 373, L36
 van der Wel, A., Holden, B. P., Zirm, A. W., et al. 2008, *ApJ*, 688, 48
 van Dokkum, P. G., Whitaker, K. E., Brammer, G., et al. 2010, *ApJ*, 709, 1018
 Visvanathan, N., & Sandage, A. 1977, *ApJ*, 216, 214
 White, S. D. M. 1976, *MNRAS*, 177, 717